

Lawrence Berkeley National Laboratory

Recent Work

Title

Broadening the Application Range of NMR and MRI by Remote Detection

Permalink

<https://escholarship.org/uc/item/8j4182gt>

Authors

Han, Song-I.
Granwehr, Josef
Hilty, Christian

Publication Date

2006

Broadening the Application Range of NMR and MRI by Remote Detection

Song-I Han¹, Josef Granwehr² and Christian Hilty²

¹ Department of Chemistry and Biochemistry, University of California Santa Barbara, CA 93106-9510, USA

² Lawrence Berkeley National Laboratory, Materials Sciences Division, and University of California Berkeley, Department of Chemistry, Berkeley CA 94720, USA

NMR remote detection is a new technique in which the signal detection location is physically separated from the sample location where NMR or MRI information is encoded. A mobile NMR-active sensor medium (*or: nucleus*) interacts with the host sample without altering it, and information of that sample environment is encoded with radio frequency (rf) and field gradient pulses as longitudinal magnetization of the sensor. After the sensor has left the sample, its magnetization is read out with an optimized detector, which often can be made much more sensitive than the circuit used to encode the information. Remote detection fully capitalizes on the unique strength of NMR —the wealth of encoding possibilities—, while providing a means to overcome its inherent weak point —the low sensitivity.

1. Motivation

NMR spectroscopy and magnetic resonance imaging (MRI) techniques are most powerful and versatile in providing information about atomic and macroscopic structures over a large length and time scale. Chemical constitution and molecular conformations can be reconstructed, rotational and translational dynamics measured and thermal diffusion, coherent flow and macroscopic densities mapped. However, NMR techniques are intrinsically insensitive compared to other analytical and visualization tools. One reason is that for a thermally polarized sample even at high field, only a few ppm of the total number of NMR-active nuclei contribute to the overall signal. Furthermore, conventional rf detection scales unfavorably for use with large, bulky sample volumes and low magnetic fields. Much effort has been invested to seek for techniques that provide for higher nuclear spin polarization and higher signal detection efficiency to overcome this sensitivity limitation. High magnetic fields would serve both aspects (the signal-to-noise ratio scales with $B_0^{3/2}$, where B_0 is the static magnetic field), however the upper limit field strength for commercially available NMR magnets lies currently at 21 Tesla. Various hyperpolarization techniques [1-6] can provide percent-range nuclear polarization, with signal enhancements of several orders of magnitude. Cryo-cooled rf circuits give about 4 times higher detection sensitivity [7], and when working with nanoliter to microliter range sample volumes,

advantage can be taken of the better mass sensitivity offered by rf microcoils [8-10]. However, most of these techniques are only applicable to specific nuclei and samples or enhance the detection sensitivity only by a small factor despite a considerable cost factor. An important consideration for making NMR and MRI applicable for applications in chemical engineering is to provide for flexibility in handling samples of various sizes, materials, shapes, or temperatures, while ensuring sufficiently high NMR detection sensitivity. In this chapter, we present a novel technique called NMR and MRI remote detection [11, 12] that addresses these problems in a fundamental fashion, as well as a few examples where remote detection has been applied successfully.

2. Principle of NMR Remote Detection

2.1 Spatial Separation of NMR Encoding and Signal Detection

The idea of NMR remote detection is to spatially separate the encoding of information about a sample from the detection of the signal. The information is stored as longitudinal magnetization M_z of a mobile sensor medium, which can be transferred between the sample and the detector (Fig. 1). The encoding is technically optimized to provide for high quality of the encoded information, while the detector is optimized to measure M_z as sensitively as possible. The sample is not confined anymore to conditions that meet both high encoding quality and detection sensitivity. Optimizing for high detection sensitivity in conventional NMR or MRI typically means using high magnetic fields and small volume rf coils. On the other hand, conditions for optimized encoding include a good rf and magnetic field homogeneity, a sufficiently large rf coil

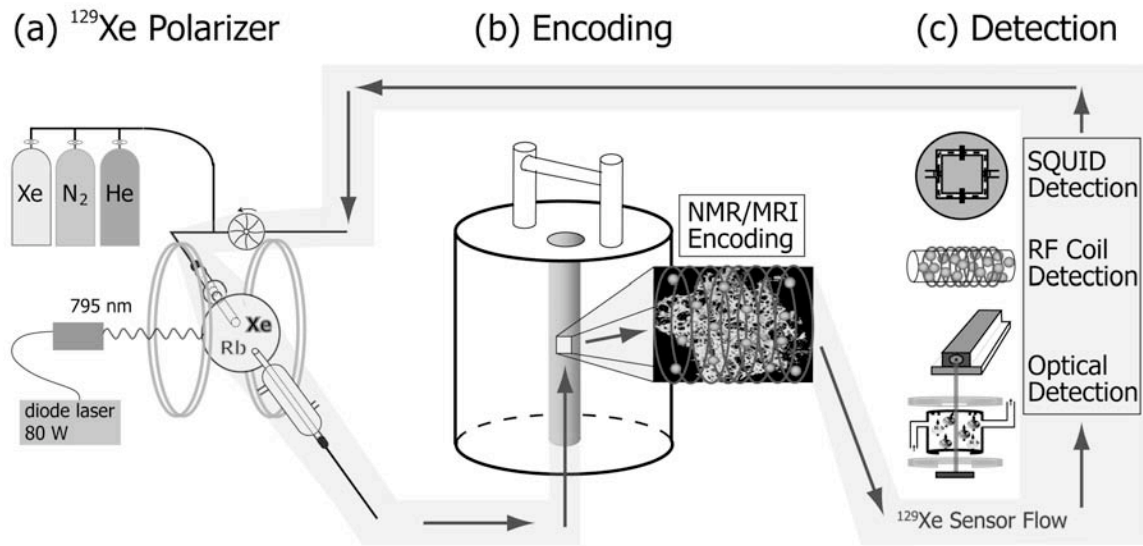


Figure 1: Schematic of an experiment with remote detection. The basic steps are the polarization of the sensor medium (a), NMR or MRI encoding using rf pulses and magnetic field gradients (b), and signal detection (c). The NMR or MRI information travels between the locations (b) and (c).

volume to encompass bulky samples, and low magnetic fields if samples with large susceptibility gradients due to paramagnetic impurities and metallic components are to be imaged.

Since remote detection spatially separates the detection from the encoding, optimized detection can be realized by a variety of means to sensitively read out M_z . Detection can be done not only by an rf coil of optimized size – the detection sensitivity is inversely proportional to the coil diameter [8-10] –, but also by alternative methods or devices. Examples for the latter include Superconducting Quantum Interference Devices (SQUIDs) [13, 14], spin-exchange optical detection [2], or atomic magnetometers [15-17] (Fig. 1). This approach to optimize encoding quality and detection sensitivity individually by transporting only the NMR information, but not the sample itself to the detector can enhance the sensitivity of NMR and MRI by orders of magnitude.

2.2 NMR Information Carrier

The question to be answered next is how the NMR information about the sample is being stored and carried to the detection location. The information can be transported by any fluid that has NMR active nuclei with a sufficiently long spin-lattice relaxation time, T_1 , to enable reading out the encoded information after the time of travel to the detector. Furthermore, the carrier should be chemically inert so that it does not alter the sample when passing through. Depending on the application, the distance that the carrier travels during this time can span a wide range from tens of millimeters to several meters. A variety of nuclei are suitable to act as NMR signal carriers, among them laser-polarized ^3He or ^{129}Xe gas [1, 2], ^{13}C nuclei of solvents or ^1H nuclei of oil or water. T_1 of the listed carriers decreases in the order in which they are named. If not in contact with any relaxation causing substance or surface, this is up to 40 hours for ^3He , tens of minutes for ^{129}Xe gas, and a few seconds for ^1H of water. Accordingly, the covered travel distances can range from many meters down to only a few millimeters, depending on the choice of the carrier. The long-living inert noble gases ^3He or ^{129}Xe have to be laser-polarized in order to deliver high initial polarization, whereas for the shorter living ^1H of water, sufficiently high thermal polarization is achieved in the presence of magnetic fields with medium to high strength. This discussion also shows that the carrier can be in the gas or in the liquid phase, so that complex flow properties of the carrier itself through porous samples can be studied.

Depending on the choice of the carrier medium, NMR spectra as well as NMR images can be remotely detected using the same basic principle which will be discussed shortly. However, for remote detection of NMR spectra, the information carrier has to fulfill one more criteria. It has to show a chemical shift upon non-covalent contact with the sample environment. Thus, differences in surface chemistry, pore size or other physicochemical properties of the material can be detected. The best candidate nucleus from this point of view is ^{129}Xe , and other nuclei such as ^{15}N and ^{13}C also have potential to serve as sensor atoms, given that mechanisms for hyperpolarization are developed to overcome the signal limitation due to their low density, low natural abundance, and low gyro-magnetic ratio. The spin polarization of ^{129}Xe can be enhanced

by 3-5 orders of magnitude relative to thermal polarization by Rb-Xe spin exchange optical pumping using circularly polarized laser light with the frequency of the Rb D_1 line [1, 2]. Figure 1 schematically shows the basic steps of remote detection when using continuous-flow laser-polarized ^{129}Xe gas as the information carrier. All example data presented in this chapter use this fundamental scheme.

The most basic experimental manifestation of travel of information can be obtained by tracing the flow of tagged spins from the encoding to the detection location. The spins in the encoding coil are tagged by applying a π -pulse to invert the ^{129}Xe magnetization. Subsequently, the arrival of the traveling spins is continuously monitored at the detection location by repeated pulsing and the subsequent recording of the free induction decay (FID) at the detection coil. An example of a travel time curve obtained in this way is shown in Fig. 2. At short times after the tagging, the spin-encoded fluid packets have not yet reached the detector, therefore the detection signal shows maximum intensity. When encoded fluid starts to reach the detector, the signal intensity gets reduced, finally showing a negative intensity. Later the signal slowly recovers to its maximum. The signal never reaches an inverse value of the unencoded signal in this example mainly due to dispersion and mixing with unencoded spins (positive amplitude), but also because of a not perfectly homogeneous rf field, B_1 , and the corresponding inhomogeneous distribution of flip angles of the tagging pulse, which is a common problem with large encoding volumes.

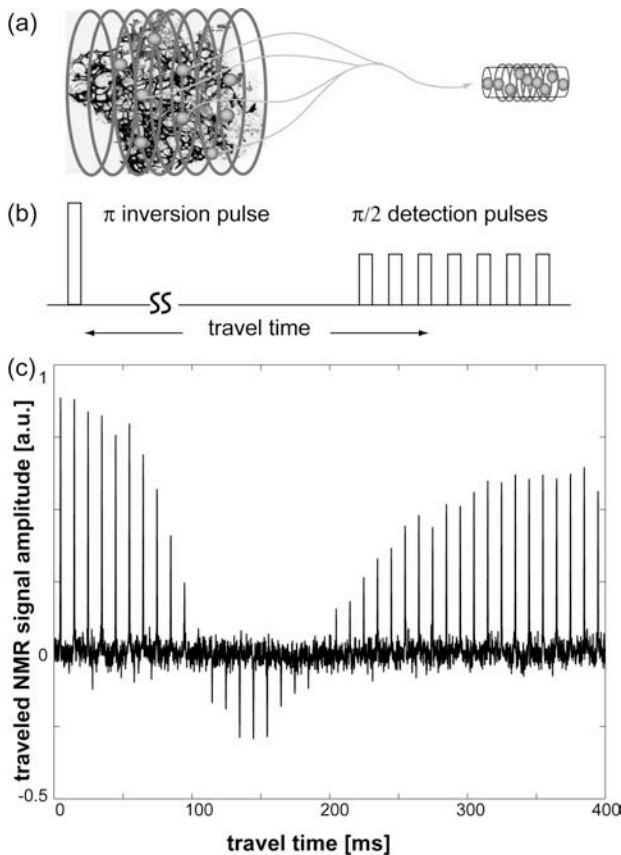


Figure 2: Transportation of tagged spins from the encoding rf coil to the detection rf coil using a remote detection setup (a). Basic pulse sequence used to invert the magnetization of spins in the encoding coil, and subsequently to detect the magnetization at the detector location as a function of the travel time (b). A typical travel time curve where encoding and detection were done at high field inside the same magnet (c).

2.3 Encoding and Reconstruction of NMR and MRI Information

In general, a detectable NMR signal is induced by transverse magnetization that precesses coherently with characteristic amplitude and frequency distributions in response to the applied pulse sequence, a tailored series of rf and gradient pulses. Any NMR signal that can be observed directly as a transient signal during an evolution time t_2 can also be *indirectly* read out in a point-by-point fashion. When using remote detection, at each time increment, t_1 , during precession, a projection of the magnetization along the x or y axis is stored as longitudinal magnetization using a $\pi/2$ storage pulse. As such, it is not affected by dephasing due to the presence of inhomogeneous magnetic fields. Then, it is physically transported to the detector during the travel time, where its amplitude is read out. Both the x and the y components of the magnetization can be obtained in two subsequent experiments and constitute one complex point of the NMR signal. This procedure is repeated for every time evolution increment t_1 , and the series of the signal points collected corresponds to the indirectly detected NMR signal in the time domain. Its Fourier transformation (FT) is the reconstructed NMR spectrum or image, depending on the applied pulse sequence. One drawback is that the indirect acquisition inherently adds one dimension to the remote experiment. However, as discussed above, in many cases this is outweighed by a large gain in sensitivity due to the optimized detection, whether it is achieved conventionally with an inductive coil or by other means. When using inductive detection, the bandwidth of detection can be narrowed, for example, by the application of pulse sequences such as spin lock detection [18] or the use of multiple echoes with pulse train refocusing [19] which can considerably enhance the detected signal. This is possible because in the detected dimension, the signal amplitude, and not the frequency, carries the indirectly detected frequency information.

To demonstrate these principles, the remote detection of the spectrum of ^{129}Xe gas adsorbed to the surface of aerogel crystal fragments is presented [11]. The encoding rf coil encompasses the sample, laser-polarized ^{129}Xe gas passes through and is detected as it travels to the detection rf coil. Both coils are contained in the same magnetic field and are built into the same NMR probe (Fig. 3a). Fig. 3b shows the ^{129}Xe spectrum of the sample detected directly in the encoding coil. It contains peaks for the free ^{129}Xe gas and the ^{129}Xe adsorbed inside the 100 Å small aerogel pores. Fig. 3c correlates the transiently detected signal in the detection coil with the remotely reconstructed ^{129}Xe spectrum of the sample. The inset of Fig. 3c shows the amplitude modulation of the detected signal in the indirect dimension of the remote data, which contains the spectral information from the location of the sample. These experiments show the feasibility of remote detection as a conceptually new approach to address the sensitivity limitations in NMR spectroscopy.

3. Sensitivity Enhancement by Remote Detection

The separation of encoding and detection allows the use of different types of detectors. While at high field it might be most convenient to use pulsed or continuous wave inductive detection, where sensitivity improvements could originate from the possibility to concentrate the sensor

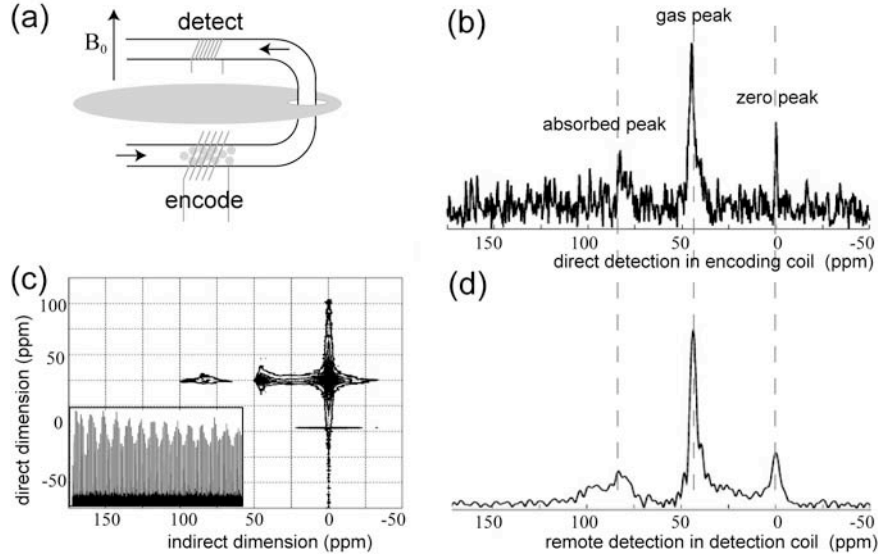


Figure 3: a) Setup for remote detection with two rf coils, one coil containing an aerogel sample where ^{129}Xe spectroscopic information is encoded, and a detection coil through which the signal carrier passes. b) ^{129}Xe spectrum, directly detected in the encoding coil obtained with one $\pi/2$ pulse and one signal acquisition. c), d) Remotely detected spectrum. The amplitude modulation of the signal arriving at the detector along the indirect dimension (inset in (c)) gives after FT the spectrum from the sample location (d). The transiently detected signal arriving at the remote detector consists of only one peak for pure ^{129}Xe gas [11].

spins into a smaller volume than the encoding volume, at low fields alternative detection methods like spin-exchange optical detection [2] or magnetometers [13, 17] might be preferred. The discussion of the sensitivity of remote detection can be split into a detector independent part that only includes the relative sensitivity between the remote detector and the circuit that is used for encoding, and a detector dependent part that discusses the ability of the different detectors to measure the polarization or the magnetic moment of the sensor spins.

3.1 Detector-independent sensitivity

The most fundamental aspect of a sensitivity discussion of remote detection is the fact that it is inherently a point-by-point technique. Each spectrum recorded by the detector does not contain any information other than its amplitude. Conceptually, a remote NMR experiment is very similar to a 2D NMR experiment with a z filter between encoding and detection, which causes all transverse magnetization to dephase. For 2D NMR experiments, it has been shown that the signal-to-noise ratio (SNR) per square root time, which will be denominated as sensitivity in the following, is the same as in the 1D case under optimal conditions [20, 21]. To compare the sensitivity of a remotely detected spectrum (Fig. 4b) with an equivalent experiment with direct detection (Fig. 4a), we can use an expression similar to the discussion in [20]

$$\begin{aligned}
\left(\frac{\text{remote sensitivity}}{\text{direct sensitivity}}\right)_{\text{NMR}} &= \frac{\Lambda}{\sqrt{2}} \sqrt{\left[\frac{t_r^{\max}/\tau_r}{t_d^{\max}/\tau_d}\right] \left[\frac{1}{t_r^{\max}} \int_0^{t_r^{\max}} [s_r^e(t_r)]^2 dt_r\right]} \\
&= \frac{\Lambda}{\sqrt{2}} \sqrt{\frac{t_r^{\max}/\tau_r}{t_d^{\max}/\tau_d}} \sqrt{\frac{T_2^r}{2t_r^{\max}} \left(1 - \exp\left(-\frac{2t_r^{\max}}{T_2^r}\right)\right)} \approx \frac{\Lambda}{\sqrt{2}} \sqrt{\frac{T_2^r}{t_d^{\max}}}
\end{aligned} \tag{1}$$

τ_d and τ_r are the recycle delays and t_d^{\max} and t_r^{\max} are the detection times in the direct and the remote experiment, respectively [22]. Λ is the relative sensitivity between the remote detector and the encoding circuit. $s_r^e(t_r) = \exp(-t_r/T_2^r)$ is the envelope of the signal in the remote detection dimension, which decays with T_2^r . Because the encoding dimension of the remotely detected experiment samples the same data points as the direct experiment, the signal decay in the

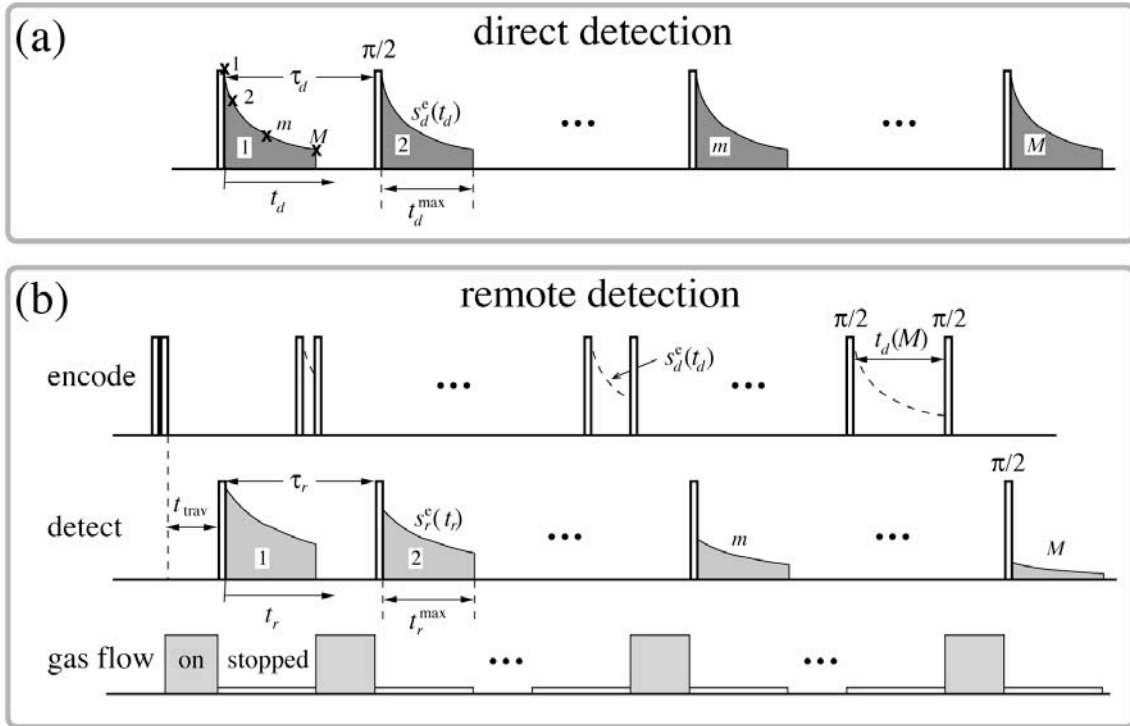


Figure 4: Sensitivity comparison between direct (a) and remote detection (b). With direct detection, an FID is recorded transiently with M data points, which are marked with 'x' symbols in the first FID in (a). Remotely, M encoding steps are necessary to obtain the same data set, which allows one to perform M signal averaging steps in the direct dimension in the same time. The encoding and detection steps in the remote experiment are intermingled, therefore only a time overhead corresponding to one travel time occurs, which will be neglected. The stored magnetization of the mth encoding step corresponds to the mth data point with direct detection and marks the magnetization at the beginning of the remote detection. The sensitivity is proportional to the total area under all the FIDs in both cases. With identical detectors, we would get an equal sensitivity with remote detection only if the remote signal would not decay.

encoding volume, $s_d^e(t_d)=\exp(-t_d/T_2^d)$, cancels from the sensitivity ratio. A matched filter for optimum sensitivity in the remote dimension was assumed, which causes the bandwidth of the detection to be $\Delta f=4/T_2^r$. The factor $1/\sqrt{2}$ in Eq. (1) is because only one component of the transverse magnetization can be stored and read out at a time with remote detection, requiring two cycles to obtain the complex signal. t_d^{\max}/τ_d and t_r^{\max}/τ_r represent the duty cycle in the remote and the direct experiment, respectively. For the approximation it was assumed that $\tau_d=\tau_r$ and $t_r^{\max}>T_2^r$. As is visualized in Fig. 4, if $\Lambda=1$ and the number of signal averaging steps of an experiment with direct detection is equal to the number of points detected indirectly with remote detection, the relative sensitivity is given by the integral of all the remotely detected signals relative to the integral of all the directly detected signals. An equal sensitivity is obtained only if the remote signal does not decay during detection, because plain signal averaging in the direct dimension also does not show any signal decay and has therefore an infinitely narrow bandwidth.

The situation is different in an experiment where the acquisition dimension of the conventional, direct detection experiment itself measures only the magnitude of a signal, as opposed to its time evolution. This is the case for example in an MRI experiment with phase encoding in all three dimensions. Here, it is the 1D sensitivity that has to be compared between remote and direct detection, because the direct FID is not anymore sampled point-by-point. Also following the treatment of 1D sensitivity in [20], this yields

$$\begin{aligned} \left(\frac{\text{remote sensitivity}}{\text{direct sensitivity}} \right)_{\text{MRI}} &= \frac{\Lambda}{\sqrt{2}} \sqrt{\frac{\left[\frac{t_r^{\max}}{t_r} / \tau_r \right] \frac{1}{t_r^{\max}} \int_0^{t_r^{\max}} [s_r^e(t_r)]^2 dt_r}{\left[\frac{t_d^{\max}}{t_d} / \tau_d \right] \frac{1}{t_d^{\max}} \int_0^{t_d^{\max}} [s_d^e(t_d)]^2 dt_d}} \\ &= \frac{\Lambda}{\sqrt{2}} \sqrt{\frac{\frac{T_2^r}{\tau_r} \left(1 - \exp\left(-\frac{2t_r^{\max}}{T_2^r}\right) \right)}{\frac{T_2^d}{\tau_d} \left(1 - \exp\left(-\frac{2t_d^{\max}}{T_2^d}\right) \right)}} \approx \frac{\Lambda}{\sqrt{2}} \sqrt{\frac{T_2^r}{T_2^d}} \end{aligned} \quad (2)$$

For the approximation it was again assumed that $\tau_d=\tau_r$ and $t_r^{\max}>T_2^r$, $t_d^{\max}>T_2^d$. A comparison between Eqn. (1) and (2) shows that the potential signal advantage of remote detection in the case of imaging experiments is considerably larger than for spectroscopy experiments because for imaging, the bandwidth of the direct experiment is determined by the decay time and not by the signal averaging. This is particularly important for samples with large susceptibility gradients, which cause fast dephasing of the transverse magnetization.

In the above calculations it was assumed that all of the sensor medium gets fully regenerated between different repetitions of the experiment, which is reasonable because it is not a T_1 decay that determines this “relaxation”, but a flow that forces the encoded sensor to move ahead. Furthermore, multiplicative noise, or t_1 noise, was not considered. Depending on the type of experiment, this noise source can have a considerable influence on the sensitivity [22-25].

Another factor that has been left out is longitudinal relaxation of the sensor medium between encoding and detection. This simply causes the remote sensitivity to be multiplied by a factor $\exp(-t_e/T_1)$, which is close to unity for ^{129}Xe , but can be considerably smaller for a different sensor medium. Another aspect that has not been covered is that the sensor medium could disperse between encoding and detection, and thereby being diluted with unencoded fluid. This would either require a detector with a bigger active volume so still all the encoded fluid can be read out in one experiment, or it requires multiple experiments to catch all the encoded gas. In the case of a spectroscopy experiment without spatial dependence of the encoded information, it is not required to gather all the encoded fluid, and the signal would just be scaled proportionally to the amount of encoded fluid in the detector. But if spatial information is encoded, it is required that the entire encoded sensor medium is detected. If it is diluted, the sensitivity is reduced, but the image can still be reconstructed accurately. However, if some of the encoded fluid remains undetected, the image will be weighted unevenly.

In experiments where the flow of the sensor medium is studied transiently, an additional decay of the signal is present due to the continuous flow of the fluid out of the detector. In a first approximation, this effect, which depends on the flow rate and the detector volume, may also be included in the apparent transverse relaxation time T_2^r , and the above formulae can be applied to estimate the sensitivity. If detection is done inductively with a train of n pulses, typically the time between subsequent detection pulses should be chosen no less than $2T_2^r$ to maintain good sensitivity and avoid artifacts. To increase the temporal resolution of the flow detection further, the detector volume has to be reduced. If the number of acquisitions n is increased, the noise of the integrated signal will scale with \sqrt{n} . On the other hand, the smaller detection volume allows for a more sensitive coil, again compensating for the lost sensitivity. These parameters all have to be considered when designing a remote NMR acquisition system. However, this calculation does not take into account the potential gain of information by such an experiment, which will be demonstrated in section 4.3. Furthermore, if phase encoding is done in the flow direction of the sensor medium, it is possible that the sinusoidal pattern of the longitudinal magnetization after the storage pulse is preserved during the flow. If the temporal resolution of the detection is fast enough to resolve this pattern, the sensitivity could be somewhat recovered. But this strongly depends on the sample object to be studied and is outside the scope of this discussion.

3.2 Optimized rf coil detection

In order to use Eqn. (1) and (2) to estimate the sensitivity gain obtained by remote detection, knowledge of the relative sensitivity of the detector and the encoding circuit, Λ , is required. Here, we discuss the sensitivity for an rf coil detector as an example, because all the experiments presented in this text use inductive detection at high field. The signal-to-noise ratio of inductive NMR detection can be approximated by the following simplified equation [12]

$$(\text{SNR})_{\text{LCR}} = K\eta M_0 V_c \sqrt{\frac{Q\omega_0}{T\Delta f V_c}} = Km_0 \sqrt{\frac{Q\omega_0}{T\Delta f V_c}}, \quad (3)$$

where K is a numerical factor which depends on coil geometry, the noise figure of the preamplifier, and also takes into account various physical constants. η is the filling factor of the sample in the detection coil, M_0 is the nuclear magnetization, which takes into account the concentration of the target spins in the sample volume, V_c is the volume of the coil, Q is the quality factor and ω_0 is the resonance frequency of the rf circuit, T is the temperature of the probe, and Δf is the detection bandwidth [26-28]. Δf in a pulsed NMR experiment is inversely proportional to T_2 and has already been included in Eqn. (1) and (2). Therefore it is not discussed any further in this section. m_0 is the net magnetic moment of the spins inside the coil volume, which is transported without loss from the encoding to the detection location in an ideal remote experiment. The SNR in a remote experiment can be enhanced by optimizing the factors η , M_0 , V_c , Q , ω_0 , and T independently for the encoding and detection steps, which is not possible in a conventional NMR experiment. For example, an rf coil with better filling factor η and quality factor Q can be used for detection than may be possible for the encoding coil due to constraints imposed by the presence of the sample. A higher magnetic field can be employed for more sensitive detection (ω_0) while a lower field may be used for encoding, for example to decrease susceptibility artifacts in imaging. Or the detection coil can be cooled to enhance detection sensitivity while still preserving the optimal temperature conditions for the sample.

Finally, to estimate Λ at a given B_0 and T , it is sufficient to consider the coil's Q and V_c . The B_1 field, and thus the $\pi/2$ pulse length t_{90} , are directly related to these parameters, as expressed in [12]

$$(\text{SNR})_{\text{LCR}} \propto m_0 \sqrt{\frac{Q}{V_c}} \propto m_0 B_1 \propto \frac{m_0}{t_{90}}. \quad (4)$$

Consequently, knowledge of the t_{90} of both coils—for the same applied rf power—allows a rough calculation of the expected signal-to-noise ratio, in agreement with the principle of reciprocity [27]. The sensitivity ratio between the two coils is thus given by

$$\Lambda = \frac{(\text{SNR})_r}{(\text{SNR})_d} = \sqrt{\frac{Q_r/V_c^r}{Q_d/V_c^d}} = \frac{t_{90}^d}{t_{90}^r}, \quad (5)$$

where d and r denote the corresponding parameters of the encoding and the remote detection circuit, respectively.

4. Application of NMR Remote Detection

4.1 Broadening the application range

The possibility to detect the NMR signal remotely from the sample location in a more sensitive manner opens up a wealth of new applications. One prominent example is NMR imaging at low magnetic field [29-33], including earth field [34]. Advantages are the narrower line width in the presence of a given relative inhomogeneity, less distortion due to inherent susceptibility

variations, which occur for example at interfaces, better performance in the presence of paramagnetic and metallic objects, greatly enhanced T_1 contrast, the possibility to accommodate larger samples, and lower cost. Sensitive detection can be achieved *e.g.* by inductive detection at high magnetic field, or by using alternative detection techniques as named above, which scale more favorably at low magnetic fields. Low-field encoding together with high-field detection implies a long travel distance of the carrier nuclei between the different magnetic fields. It has already been demonstrated that NMR images encoded at magnetic fields of 4-7 mT can be accurately reconstructed at 4.2 T utilizing laser-polarized ^{129}Xe gas for transporting the encoded information over a distance of 5 meters [11]. Although high-field detection using a superconducting magnet in combination with low-field encoding is not cost-effective, new applications for NMR imaging can be opened up. A much simpler setup could be possible with a permanent magnet for detection, which can have fields up to about 1 T. The possibility of remote low field NMR imaging together with sensitive detection would free the remote detection technique from the expensive and immobile high-field NMR magnet and enable measurements outside a laboratory. Possible applications in chemical engineering include the NMR imaging and flow study on a full-size, running chemical reactor, separation column, or extraction apparatus.

Although it may appear controversial, remote detection of NMR is not uniquely applicable to large samples and reactors, but also to miniaturized microfluidic lab-on-a-chip devices [35-37]. This is because the chip device itself is large and bulky compared to the micron scale fluid channels which are embedded in it. The best sensitivity when working with such small volumes can be achieved by using microsolenoid or microsurface coils [8, 38], but a much larger rf coil is needed to encompass the entire chip device. The transportation of fluid through the channel structure is an integral part of the operation of a microfluidic chip device, which naturally fulfills the prerequisite for the application of remote detection. A possible scenario is to use a large volume coil which encompasses the entire chip for encoding, and subsequently leading the sensor molecules out of the chip into a solenoidal microcoil for detection. Common to the applications of remote detection in large and small samples is that flow is an integral part of the technique. It is not only essential for signal transportation, but can also be studied in itself, whereby unprecedented information about the flow inside of channels or porous samples can be obtained on a much broader time and length scale than is possible by conventional NMR flow imaging.

4.2 Hardware for High-field NMR Remote Detection

In order to perform NMR encoding and remote detection in high field, two rf coils need to be accommodated within the same field. The first proof of principle experiments for remote detection NMR spectroscopy and imaging have been performed with probes containing both coils at once, as can be seen in Fig. 5a and b [11, 12]. Such a design requires the construction of a new probe for each type of sample and experiment, and is therefore inconvenient. This section

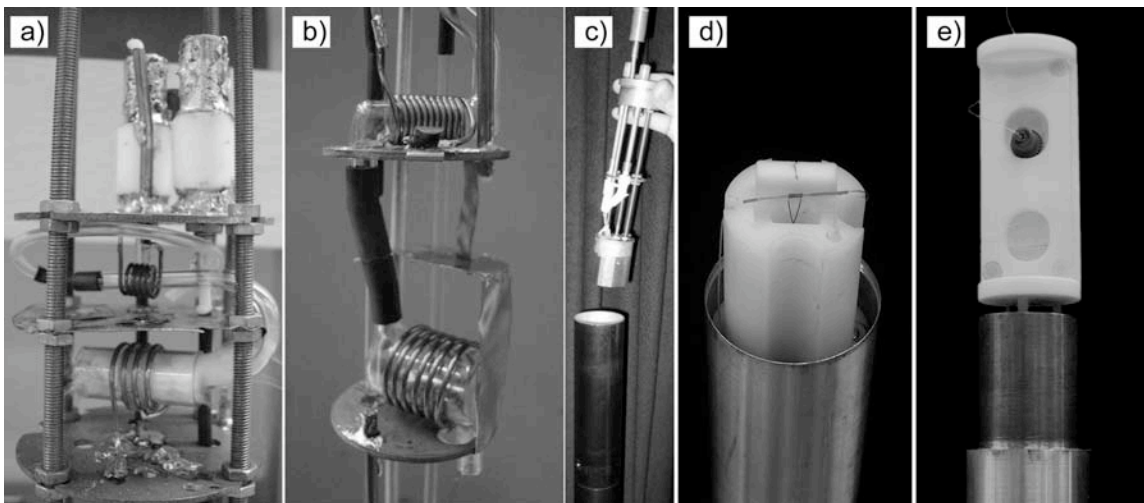


Figure 5: Hardware for high-field NMR remote detection. a) and b) show home-built remote detection probes with both rf coils built into the same body. c), d) and e) are detector-only remote probes that can be inserted from the top or bottom into the NMR imaging assembly, so that the well-shielded detection rf coil is placed immediately above or below the encoding coil. The detector probe in c) contains a relatively large saddle coil and is used for (flow) imaging. The detector probe in d) contains a micro solenoid coil for optimized mass sensitivity, which is particularly useful for microfluidic NMR applications. e) shows the same probe with a mounted holder for a microfluidic chip that is inserted into an imaging probe.

contains some general suggestions for probe hardware design, showing how remote detection can be made easily accessible for use with any high-field NMR setup [39].

Most of the commercially available NMR imaging probes have an accessible clear bore above and below the coil, which can be used for remote signal encoding. A detection-only probe can be inserted from the top into the bore of the magnet in such a way that the detection coil sits immediately above the imaging coil (Fig. 5c). Similarly, an rf probe with a narrow body can be built that can be inserted into the NMR imaging probe and gradient stack assembly from below (Fig. d,e), so that the detection coil sits just below the imaging coil. This detection-only probe can also be used together with other NMR probes with different characteristics for encoding. In all cases, care has to be taken to adequately shield and decouple the encoding and detection rf coil. In the probes presented in Fig. 5, a well grounded copper or aluminum “hat” on top of the detector serves this purpose. Both saddle coil (Fig. 5c) and micro solenoid coil (Fig. 5d) detectors have been built for ^1H , ^{129}Xe and ^{13}C nuclei and are successfully and reproducibly applied for various studies including imaging and flow studies in porous media, plants and microfluidic chip devices. The detector-only probes are optimized for highest sensitivity, but the B_0 homogeneity at the detector location may be compromised, because the two probes might be too large to fit inside of the homogeneous spot of a high-field magnet, requiring a trade-off when shimming the

magnet. Coils with the axial direction along the B_0 field would in principle be preferable to facilitate transport of the carrier nuclei in a straight tube from the encoding coil to the detector coil, but are not always easiest to manufacture and suffer from a somewhat lower sensitivity compared to solenoid coils [26].

Low field encoding coupled with high field or non-inductive detection requires a separate design. Presently, considerable effort is being devoted to developing and implementing low field and ultra low field NMR and MRI equipment [29-34]. A few examples are reviewed in this book (chapters 1.2-1.4). There is no principle obstacle to couple these possibilities to design commercially available remote NMR and MRI equipment for low field studies.

4.3 High-field NMR Imaging with Remote Detection

In this example, high-field remote detection NMR imaging of a phantom with the engraved letters “CAL” is performed with a continuous flow of a gas mixture containing 1% of xenon with natural isotope abundance. It is demonstrated how a non-uniform flow pattern can influence the resulting image features, but also how in spite of this an image without distortions can be reconstructed. In particular, the non-uniform flow pattern and a mismatch in the sample volumes of the encoding and detection cell lead to a partitioning of the encoded gas volume. If individual partitions are separately detected and Fourier transformed, parts of the image are obtained corresponding to the respective time of travel, as shown in the right part of Fig. 6. However, if the detection steps are repeated over a time period sufficiently long to collect all the information in several batches, the complete image can be recovered, as can be seen in the left image of Fig. 6. The spreading of the transported signal along the flow path in remote detection is not necessarily reflected in a degradation of the image quality, as long as the entire signal is collected to complete an

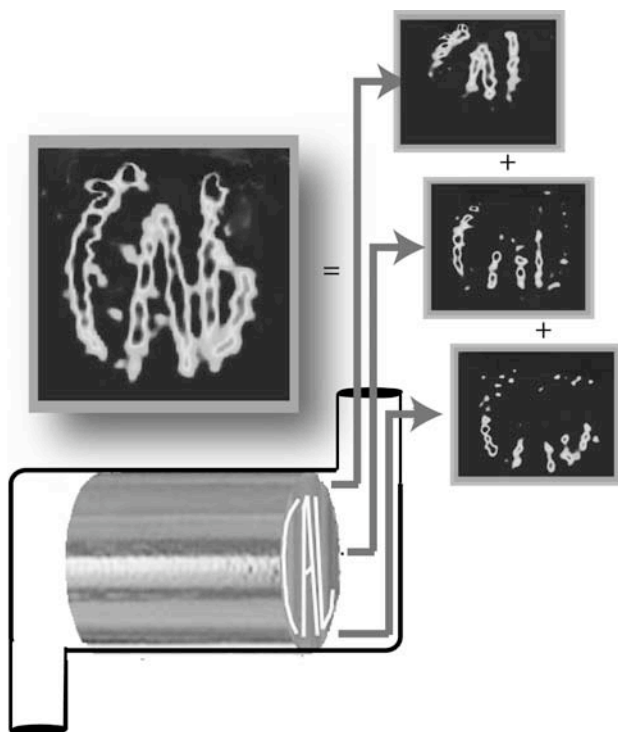


Figure 6: Remotely reconstructed high-field NMR images of laser-polarized ^{129}Xe gas in the hollow „CAL“ pores. Due to the flow pattern where the spins have to flow around two corners (see probe design in Fig. 5b, earlier batches of spins reconstruct the upper part and later batches the lower part of the porous sample. After all batches are added up, a complete image is reconstructed [12].

individual signal point in the k -space. However, a distorted flow path lengthens the experimental time. The experimental time may be vastly reduced, while improving the sensitivity and resolution, by utilizing fast pumping or injection devices and employing stop-and-go flow control systems. A similar approach can be used not only to recover the image of an object, but in addition to study properties of the flow itself in a unique fashion, as discussed in the next section.

4.4 Flow Detection and Visualization

The flowing sensor medium as an integral part of remote detection naturally leads to the study of flow through porous media [40,41]. In addition to carrying the information about an image of the sample, as in the previous section, the arrival of the encoded sensor in the detector depends on the flow properties and the flow path of the gas through the entire object [42]. Therefore it permits characterization of flow with a time-of-flight (TOF) experiment [43], the principle of which is shown in Fig. 7a. The difference to an experiment where remote detection is used solely for sensitivity optimization is that in the present case, the detection volume is typically chosen smaller than the effective void space volume of the sample to improve the temporal resolution. Also, the encoding and the detection volume should be placed as close to each other as possible to avoid additional dispersion of the flowing sensor medium outside of the sample. If detection is done inductively, for example using a probe of the same type as the one depicted in Fig. 5c, a pulse train can be used as shown in Fig. 2b to stroboscopically sample the magnetic moment of the spins inside the detection volume. Because the chemical shift of the sensor signal in the detector is known, continuous wave detection is also possible. In combination with MRI encoding [44], the dispersion curve for a fluid in each volume element of the sample can be measured. A general pulse sequence is shown in Fig. 7b. Since the flow between encoding and detection removes any transverse magnetization, only one data point can be encoded spatially at a time, but provided that the temporal resolution of the detection technique is fast enough, the complete TOF curve for the sensor can be recorded transiently for each encoding step. This experimental approach to measure hydrodynamic dispersion is similar to the technique of an initial narrow-pulse tracer injection, with the subsequent observation of the effluent concentration of the tracer [42,45]. The difference is that using MRI techniques the point of injection can be defined non-invasively anywhere inside the porous medium. Equally important is that the spin magnetization behaves like an ideal tracer, as it does not affect the properties of the flowing medium.

Two fundamentally different approaches are possible for encoding. One employs slice selective pulses to only modify the polarization of the sensor medium as a function of position. The other uses phase encoding, where transverse magnetization, M^+ , coherently precesses for a given time under the influence of magnetic field gradients, followed by a 90° storage pulse to transfer one component of M^+ to longitudinal magnetization, M_z , which is resistant to all types of decays but T_1 relaxation as it flows or diffuses through inhomogeneous magnetic fields. This second scheme, which employs a storage pulse, in principle allows using any desired encoding sequence. The approach with a slice-selective pulse only, on the other hand, can be used for

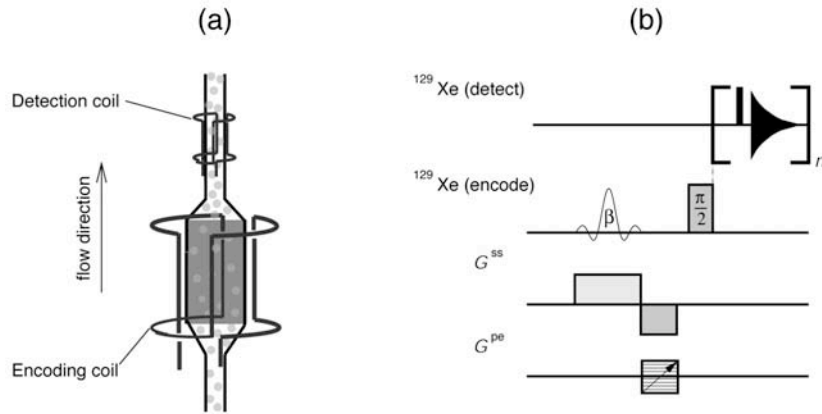


Figure 7: General principle of time-of-flight flow detection. a) Schematic of a setup for TOF experiments. An object of interest is placed inside an environment optimized for encoding (field gradients not shown). As the sensor medium flows out of the analyte object, its magnetization is recorded with a second coil with a smaller volume that is placed as close to the encoding volume as possible. b) Generic pulse sequence used for TOF experiments. Encoding along one dimension can be done by inverting the magnetization of a slice through the sample. In this case, β is 180° , and no storage pulse is needed. For 2D encoding, a selective pulse with $\beta=90^\circ$ and a bipolar field gradient G^{ss} is used for slice selection in one dimension, and phase encoding gradients G^{pe} are used to resolve the other spatial dimensions. 3D encoding can be done with a hard 90° preparation pulse and phase encoding in three dimensions. The spacing between the n detection pulses defines the temporal resolution of the TOF experiment.

encoding even if M^+ dephases too fast to allow for phase encoding, for example if a sample with large susceptibility gradients is to be characterized in a high magnetic field.

An example for gas flow using hyperpolarized ^{129}Xe gas in a mixture of 1% Xe (natural isotope abundance), 10% N_2 , and 89% He through a cylindrical glass phantom is shown in Fig. 8. Encoding was done with slice-selective pulses to invert the magnetization of slices either perpendicular or parallel to the flow direction. The sample was scanned by changing the rf offset frequency of the inversion pulse. The magnetization was detected with a train of 90° pulses, spaced by 100 ms. Each slice was recorded four times, with the position of the detection pulses shifted by 25 ms between subsequent experiments. This interleaved data acquisition allowed for a smoother representation of the TOF data and corresponds to signal averaging, but as long as the time between detection pulses is not longer than the time it takes the sensor medium to flow through the detection volume, the temporal resolution is not improved. In the experiment with slice selection parallel to the flow direction, the data is not perfectly symmetric, as would be expected from the symmetry of the sample. This is because the z gradient coils were designed for smaller samples, and the phantom reaches outside the linear region of the gradients. In the experiment with the inverted slices perpendicular to the flow direction, the slope of the data in

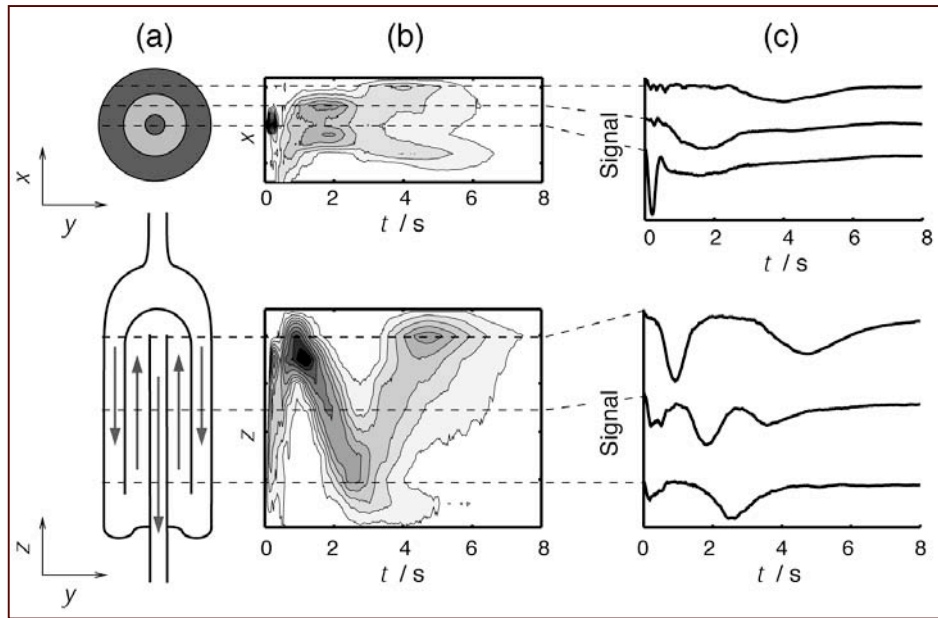


Figure 8: Time-of-flight dispersion curves vs. encoding position of gas flowing through a cylindrically symmetric glass phantom with large „pores“ on the order of 1 cm diameter, obtained with slice selective inversion of magnetization. The flow direction changes twice as the gas is flowing from inlet to outlet. Slices parallel (upper) and perpendicular (lower) to the flow direction were inverted. a) Cross-section of the object perpendicular to the inverted slices. The arrows in the lower graph depict the direction of the gas flow. b) Contour plots of the signal. c) TOF signal of selected slices, as indicated by the dashed lines.

Fig. 8b corresponds to the flow velocity of the gas. As can be seen in Fig. 8a, the flow in this object changes its direction twice, which is reproduced in the flow curve. At the turning point at a TOF of about 3 s, a splitting of the flow in two branches can be observed, indicating that the gas does not get homogeneously mixed at this point, but that one fraction of the gas flows along a relatively well defined path, while a second fraction gets trapped in an inactive volume with only slow exchange.

The understanding of mass transfer in porous media is highly relevant not only for the oil and gas industry, but also for process control or in chromatographic columns. While corresponding NMR techniques have been developed and successfully used for the study of liquids (e.g. [40,44,46]), measurements of diffusion and flow of gases in porous media are still challenging [47-49] (see also chapters 2.5 and 5.3 for references). In the next example, gas flow and dispersion in a porous Bentheimer sandstone rock is visualized. The same gas mixture as above was used. The rock was cylindrically shaped with a height of 39 mm and a diameter of 24 mm. It had an effective porosity of about 15%, and its pore size was on the order of 100 μm . The full three-dimensional space was resolved using phase encoding. No signal averaging was done, except for a four-step phase cycle to subtract the baseline, because M_z of ^{129}Xe reaches a

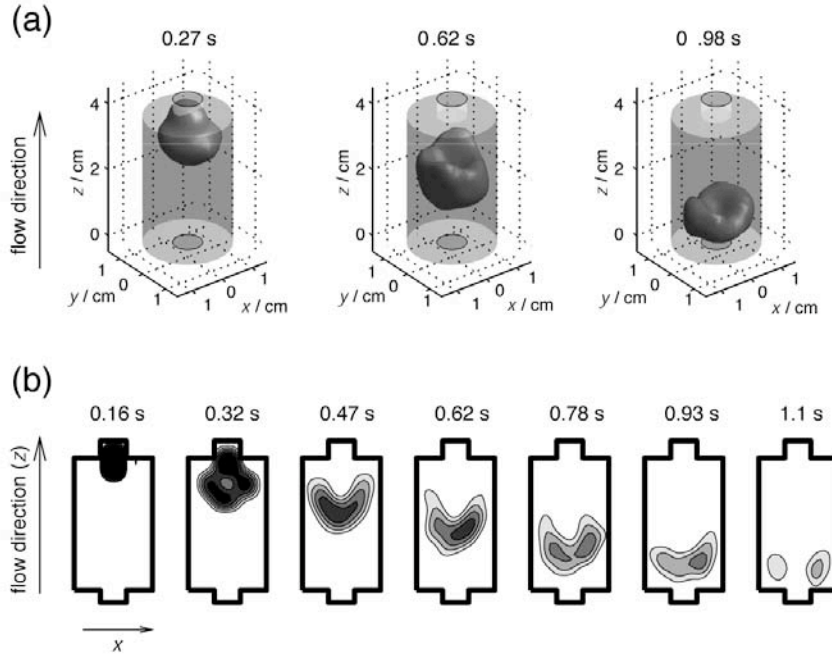


Figure 9: Visualization of gas flow through a porous sandstone rock. A 3D phase encoding sequence with a hard encoding pulse was used. a) 3D representation of an isochronal surface at different times after the encoding step. The cylindrical surface represents the rock. b) Only a slice through the center of the rock is displayed, showing the origin of the gas that is flowing through the detector at different times after the tagging.

maximum in the absence of encoding, and to obtain frequency discrimination, because only one component of M^+ is retained with each storage pulse [25]. In Fig. 9 the isochronal regions, *i.e.* areas of the rock from where it takes the gas an equal amount of time to reach the detector, are displayed. Figure 9a shows a 3D representation, indicating that despite the homogeneity of the rock the flow is neither perfectly homogeneous nor symmetric. However, there are no regions either that are blocking the flow path. Figure 9b shows a slice through the same data in a 2D diagram. One can see that mass flow is present through the entire cross-section of the rock sample without interruption except near the walls. No channeling could be observed. The observation that the regions surrounded by the contour lines do not get significantly broader for longer distances between the position where the sensor medium was encoded and the detector indicates that dispersion of the gas inside the rock is low.

This data shows the great potential of remote detection especially for flow studies, where the loss of a transient spectral or spatial dimension is compensated by a transient flow dimension. If T_2^* of the mobile sensor medium inside a porous object is long enough that phase encoding is possible, this technique offers unprecedented applications of MRI, because detection is done in a location with no significant susceptibility gradient, where the signal decay is basically limited by the residence time of the gas inside the active volume of the detector. Even if M^+ dephases too

quickly to allow any manipulation, it is still possible to saturate the magnetization with slice-selective pulses and observe the dispersion as a function of position, and full 3D information can be obtained with projection reconstruction, applying multiple slice-selective pulses in different directions.

4.5 Microfluidic Flow and Miniaturized Devices

Miniaturized fluid handling devices have recently attracted considerable interest and gained importance in many areas of analytical chemistry and the biological sciences [50]. Such microfluidic chips perform a variety of functions, ranging from analysis of biological macromolecules [51, 52] to catalysis of reactions and sensing in the gas phase [53, 54]. They commonly consist of channels, valves and reaction chambers that are able to handle nanoliters to microliters of fluid. To enable precise fluid handling, accurate knowledge of the flow properties within these devices is important. Due to the small channel size and the associated low Reynolds number, laminar flow is usually assumed. However, in small channels, fluid flow characteristics can be dominated by surface interactions, or viscous and diffusional effects. In many instances, devices are designed to take advantage of such properties, or exhibit geometries engineered to disrupt fluid flow, and are not necessarily amenable to modeling in a straight-forward way [55, 56]. Currently, methods used to gain experimental insights into microfluidic flow rely on optical detection of markers [57, 58]. Here, we show that NMR in the remote detection modality can be applied as an alternative method to profile flow in capillaries and microfluidic devices.

The NMR signal is acquired remotely as described in the previous section. In particular, image information is encoded into the nuclear spins of the fluid contained inside a microfluidic device. Subsequently, the fluid flows out of the chip into a capillary, where it is detected using a microcoil with an inner diameter that matches the capillary dimensions. The experimental setup contains an encoding assembly consisting of radio-frequency and pulsed field gradient coils designed for imaging of macroscopic objects (lower part in Fig. 5c). A detection probe (Fig. 5d, e) containing the microcoil is placed immediately below (Fig. 10) [59]. The benefit of using remote detection is on the one hand that it overcomes the low filling factor inside of the imaging coil, which is on the order of 10^{-5} . In the case presented here, direct NMR detection would not achieve sufficiently high SNR, while remote detection allows for the sensitive detection of the liquid or gas flowing out of the microfluidic chip device into the detector. On the other hand, through the separation of the detection and the encoding steps, remote detection enables the measurement of the time of flight for an ensemble of molecules originating at any position on the microfluidic device without additional effort. In this way, it yields time-resolved dispersion images [43].

As an example, profiles of gas flow in different model microfluidic devices are shown in Fig. 11. In order to obtain adequate signal in the gas phase, hyperpolarized xenon was chosen as the signal carrier. In the profiles, the vertical axis corresponds to a spatial dimension that is

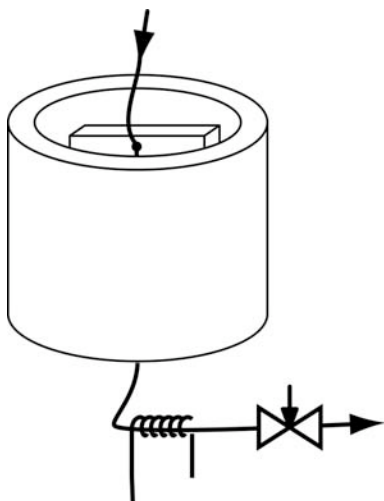


Figure 10: Specialized experimental setup for microfluidic flow dispersion measurements. Fluid is supplied from the top, flows via a capillary through the microfluidic device to be profiled, and exits at the bottom. The whole apparatus is inserted into the bore of a superconducting magnet. Spatial information is encoded by MRI techniques, using rf and imaging gradient coils that surround the microfluidic device. They are symbolized by the hollow cylinder in the figure. After the fluid has exited the device, it is led through a capillary to a microcoil, which is used to read the encoded information in a time-resolved manner. The flow rate is controlled by a home-built flow controller at the outlet [59,60].

resolved along the z -axis parallel to B_0 , and the horizontal axis shows the time of flight from the corresponding location inside of the chip. The NMR pulse sequence applied is shown in Fig. 7b, whereby for these profiles, the phase encoding option with non-selective pulses was used.

In Fig. 11a, a straight capillary with 150 μm inner diameter was profiled. The gas flow direction was from top to bottom of the figure. No divergence is observed in the dispersion curve of the capillary, indicating that under the given conditions the dispersion of flow is small, and that this scheme is thus adequate to study the dispersion within a device of interest. This may appear unexpected, as microfluidic devices usually are assumed to exhibit laminar flow, however may be explained by the fast lateral diffusion of individual gas molecules, which uniformly samples the whole cross-section of the tube in a very short time compared to the travel time. Below the image, its projection is shown together with an independently acquired overall travel curve (as in Fig. 2) that was used to determine the maximum travel time for the imaging experiment.

The profiles in Fig. 11b and Fig. 11c were obtained with a prototype microfluidic chip that had a channel depth of 55 μm , and contained a horizontal enlargement in the center, as shown by the schematic next to the experimental data. The difference between the two measurements is that in the case of b, a direct connection was used between the chip and the outlet capillary, while in c, a cylindrical mixing volume of 900 nl was present in-between. In both images, the loop of the connecting capillary is visible at low travel times. Afterwards, in b, the different flow velocities in the narrow (travel times 400–500 ms) and wide (500–700 ms) sections can directly be observed due to the different slopes. Above 800 ms, gas that remains for a long time in a mixing volume at the connection to the inlet capillary can be observed. It may be speculated whether the relative weakness of the signal at the site where the channel widens (400–500 ms and 700–800 ms) is merely due to fast flow in combination with limited spatial resolution, or due to some other effect. Very clear, however, is the difference between the images b and c. In c, a residence time of up to 300 ms can be observed at the mixing volume of the chip outlet. Moreover, in c the signal shows a forking at a travel time of 350 ms, with one part coming from

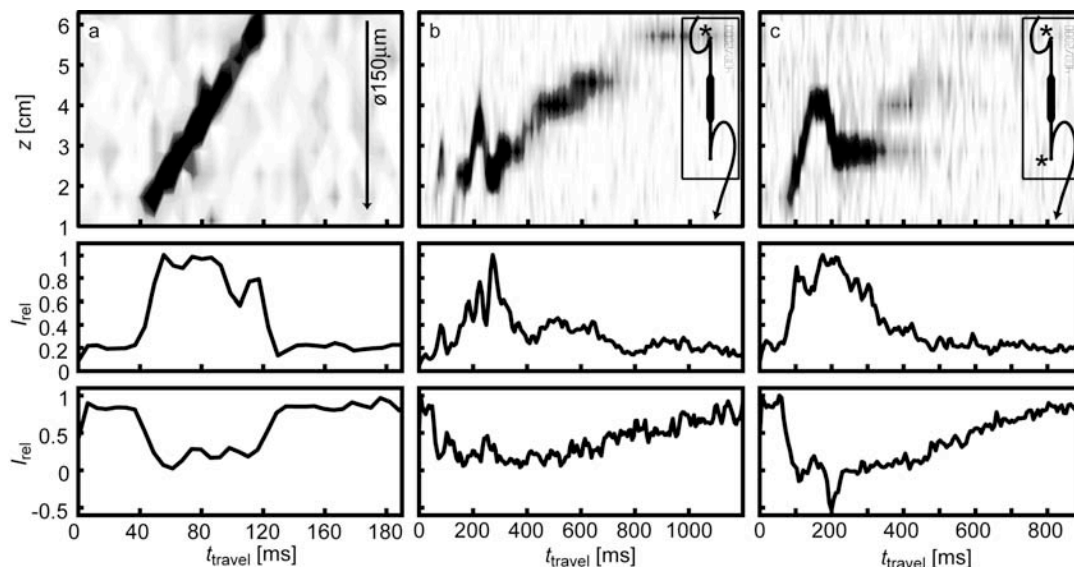


Figure 11: Flow dispersion profiles obtained with a capillary (a), with a model microfluidic chip device containing a channel enlargement, directly connected to a capillary (b), and with the same microfluidic chip connected to a capillary via a small mixing volume (c). A sketch of the model microfluidic device is placed at the right side of each image, drawn to scale along the z axis, and the presence of a cavity is marked with an asterisk (*). The flow is in the direction of the negative z -axis. Below each image, traces are plotted showing the skyline projection of the image (top), and the corresponding overall time of travel curve (bottom) [60].

the enlarged section of the channel and the other part still from the mixing volume. While one population of gas molecules passes this volume rather quickly, apparently another population remains at that point for at least twice as long, indicating a non-uniform mixing of the gas that is passing through this volume.

These examples illustrate that NMR imaging with remote detection is a viable alternative for studying flow properties inside of microfluidic chip devices. While an application to gas flow is presented here, the same experiments can be used with liquids. In the latter case, hyperpolarization is not needed due to the higher spin-density, and thus the experimental setup is further simplified. The method is only limited by the intrinsic nuclear spin-lattice relaxation time of the fluid, which needs to be in the order of seconds or more. Fortunately, this is the case for a large number of fluids, including water and organic solvents. The present approach has several advantages over other methods, like the versatility in the choice of the flow medium, the ability to work with opaque devices, and, depending on the application, the absence of the need to introduce tracer substances into the fluid flow. Foremost, however, the present method intrinsically provides additional information contained in the time-of-flight dimension, which elucidates patterns that may not be easily accessible with other methods presently available.

5. Concluding Remark

The main implications of the new remote detection methodology are the sensitivity enhancement, which can be several orders of magnitude in certain applications, the option to study flow transiently with time of flight techniques, and the broadening of the application range of NMR and MRI to samples that were previously impossible or extremely challenging to examine. Examples are large geological samples, materials with paramagnetic impurities, reactors with heterogeneous, paramagnetic catalysts or metallic components, porous media with a wide distribution of pore sizes leading to flow and image properties over a large temporal and spatial range, and bulky microfluidic chip devices interlaced with small channels. We have presented the principle and merit of the remote detection methodology on several examples, and have provided ideas for future applications in chemical engineering that can be opened up by remote detection of NMR and MRI.

Acknowledgement

We would like to thank Alex Pines for his ideas, support and continued belief in the seemingly “impossible”. A lot of all this was needed, especially at the beginning of the remote detection project. We would also like to acknowledge Juliette Seeley, Adam Moulé, Sandra Garcia, Elad Harel, Erin McDonnell, and Kimberly Pierce, whose efforts are reflected in many of the presented data, most of which are experimental results. Furthermore, we would like to thank Yi-Qiao Song for providing us with the rock sample. This work was supported by the Director, Office of Science, Office of Basic Energy Sciences, Materials Sciences and Nuclear Science Divisions, of the U.S. Department of Energy under contract DE-AC03-76SF00098.

References

- [1] W. Happer, E. Miron, S. Schäfer, D. Schreiber, W. A. Van Wijngaarden, X. Zeng, *Phys Rev. A* **1984**, *29*, 3092-3110.
- [2] D. Raftery, H. Long, D. Shykind, P. J. Grandinetti, A. Pines, *Phys. Rev. A* **1994**, *50*, 567-574.
- [3] A. Abragam, *The Principles of Nuclear Magnetism*, Clarendon Press, Oxford, **1961**.
- [4] K. H. Hausser, D. Stehlik, *Adv. Magn. Reson.* **1968**, *3*, 79-139.
- [5] A. R. Lepley, G. L. Closs, *Chemically Induced Magnetic Polarization*, Wiley, New York, **1973**.
- [6] C. R. Bowers, D. P. Weitekamp, *J. Am. Chem. Soc.* **1987**, *109*, 5541-5542.
- [7] C. Hilty, C. Fernández, G. Wider, K. Wüthrich, *J. Biomol. NMR* **2002**, *23*, 289-301.
- [8] E. W. McFarland, A. Mortara, *Magn. Reson. Imag.* **1992**, *10*, 279-288.
- [9] D. L. Olson, T. L. Peck, A. G. Webb, R. L. Magin, J. V. Sweedler, *Science* **1995**, *270*, 1967-1970.
- [10] A. G. Webb, *Prog. Nucl. Mag. Res. Sp.* **1997**, *31*, 1-42.
- [11] A. J. Moulé, M. Spence, S.-I Han, J. A. Seeley, K. Pierce, S. Saxena, A. Pines, *Proc. Natl. Acad. Sci. U.S.A.* **2003**, *100*, 9122-9127.
- [12] J. A. Seeley, S.-I Han, A. Pines, *J. Magn. Reson.* **2004**, *167*, 282-290.
- [13] K. Schlenga, R. F. McDermott, J. Clarke, R. E. de Souza, A. Wong-Foy, A. Pines, *IEEE T. Appl. Supercon.* **1999**, *9*, 4424-4427.
- [14] R. McDermott, A. H. Trabesinger, M. Mück, E. L. Hahn, A. Pines, J. Clarke, *Science* **2002**, *295*, 2247-2249.
- [15] I. K. Kominis, T. W. Kornack, J. C. Allred, M. V. Romalis, *Nature* **2003**, *422*, 596-599.
- [16] D. Budker, D. F. Kimball, V. V. Yashchuk, M. Zolotarev, *Phys. Rev. A* **2002**, *65*, 055403.
- [17] V. V. Yashchuk, J. Granwehr, D. F. Kimball, S. M. Rochester, A. H. Trabesinger, J. T. Urban, D. Budker, A. Pines, *Phys. Rev. Lett.* **2004**, *93*, 160801.
- [18] D. P. Weitekamp, *Adv. Magn. Reson.* **1983**, *11*, 111-274.
- [19] K. H. Lim, T. Nguyen, T. Mazur, D. E. Wemmer, A. Pines, *J. Magn. Reson.* **2002** *157*, 160-162.
- [20] R. R. Ernst, G. Bodenhausen, A. Wokaun, *Principles of Nuclear Magnetic Resonance in One and Two Dimensions*, Clarendon Press, Oxford, **1987**.
- [21] M. H. Levitt, G. Bodenhausen, R. R. Ernst, *J. Magn. Reson.* **1984**, *58*, 462-472.
- [22] J. Granwehr, J. A. Seeley, A. Pines, **2005**, in preparation.
- [23] A. F. Mehlkopf, D. Korbee, T. A. Tiggelman, R. Freeman, *J. Magn. Reson.* **1984**, *58*, 315-323.
- [24] J. Granwehr, *Concept. Magnetic Res.* **2005**, submitted.
- [25] J. Granwehr, J. T. Urban, A. H. Trabesinger, A. Pines, *J. Magn. Reson.* **2005**, submitted.
- [26] D. I. Hoult, R. E. Richards, *J. Magn. Reson.* **1976**, *24*, 71-85.
- [27] E. Fukushima, S. B. W. Roeder, *Experimental Pulse NMR: A Nuts and Bolts Approach*, Addison-Wesley Publishing Company, Boston, **1981**.

- [28] R. Freeman, *A Handbook of Nuclear Magnetic Resonance*, 2nd ed., Longman, Singapore, **1997**.
- [29] A. Macovski, S. Conolly, *Magn. Reson. Med.* **1993**, *30*, 221-230.
- [30] C. H. Tseng, G. P. Wong, V. R. Pomeroy, R. W. Mair, D. P. Hinton, D. Hoffmann, R. E. Stoner, F. W. Hersman, D. G. Cory, R. L. Walsworth, *Phys. Rev. Lett.* **1998**, *81*, 3785-3788.
- [31] M. P. Augustine, A. Wong-Foy, J. L. Yarger, M. Tomaselli, A. Pines, D. M. TonThat, J. Clarke, *Appl. Phys. Lett.* **1998**, *72*, 1908-1910.
- [32] R. McDermott, S-K. Lee, B. Ten Haken, A. H. Trabesinger, A. Pines, J. Clarke, *Proc. Natl. Acad. Sci. U.S.A.* **2004**, *101*, 7857-7861.
- [33] A. N. Matlachov, P. L. Volegov, M. A. Espy, J. S. George, R. H. Krauss, *J. Magn. Reson.* **2004**, *170*, 1-4.
- [34] J. Stepisnik, V. Erzen, M. Kos, *Magn. Reson. Med.* **1990**, *15*, 386-391.
- [35] J. M. Ramsey, *Nat. Biotechnol.* **1999**, *17*, 1061-1062.
- [36] D. Figeys, D. Pinto, *Anal. Chem.* **2000**, *72*, 330A-335A.
- [37] A. Groisman, M. Enzelberger, S. R. Quake, *Science* **2003**, *300*, 955-958.
- [38] C. Massin, F. Vincent, A. Homisy, K. Ehrmann, G. Boero, P.-A. Besse, A. Daridon, E. Verpoorte, N. F. de Rooij, R. S. Popovic, *J. Magn. Reson.* **2003**, *164*, 242-255.
- [39] S. Han, J. Granwehr, S. Garcia, E. McDonnell, A. Pines, **2005**, in preparation.
- [40] E. Fukushima, *Annu. Rev. Fluid Mech.* **1999**, *31*, 95-123.
- [41] J. D. Seymour, P. T. Callaghan, *AIChE J.* **1997**, *43*, 2096-2111.
- [42] J. Bear, *Dynamics of Fluids in Porous Media*, American Elsevier, New York, **1972**.
- [43] J. Granwehr, E. Harel, S. Han, S. Garcia, L. Chavez, Y. Song, A. Pines, **2005**, in preparation.
- [44] P. T. Callaghan, *Principles of Nuclear Magnetic Resonance Microscopy*, Oxford University Press, New York, **1991**.
- [45] M. H. G. Amin, S. J. Gibbs, R. J. Chorley, K. S. Richards, T. A. Carpenter, L. D. Hall, *Proc. R. Soc. Lond. A* **1997**, *453*, 489-513.
- [46] S. Stapf, S.-I. Han, C. Heine, B. Blümich, *Concept. Magnetic Res.* **2002**, *14*, 172-211.
- [47] S. L. Codd, S. A. Altobelli, *J. Magn. Reson.* **2003**, *163*, 16-22.
- [48] R. W. Mair, R. Wang, M. S. Rosen, D. Candela, D. G. Cory, R. L. Walsworth, *Magn. Reson. Imag.* **2003**, *21*, 287-292.
- [49] I. V. Koptuyug, S. A. Altobelli, E. Fukushima, A. V. Matveev, and R. Z. Sagdeev, *J. Magn. Reson.* **2000**, *147*, 36-42.
- [50] T. Chovan, A. Guttman, *Trends Biotechnol.* **2002**, *20*, 116-122.
- [51] M. A. Burns, B. N. Johnson, S. N. Brahmasandra, K. Handique, J. R. Webster, M. Krishnan, T. S. Sammarco, P. M. Man, D. Jones, D. Heldsinger, C. H. Mastrangelo, D. T. Burke, *Science* **1998**, *282*, 484-487.

- [52] D. L. Huber, R. P. Manginell, M. A. Samara, B. I. Kim, B. C. Bunker, *Science*, **2003**, *301*, 352-354.
- [53] Y. Ueno, T. Horiuchi, T. Morimoto, O. Niwa, *Anal. Chem.* **2001**, *73*, 4688-4693.
- [54] J. Kobayashi, Y. Mori, K. Okamoto, R. Akiyama, M. Ueno, T. Kitamori, S. Kobayashi, *Science* **2004**, *304*, 1305-1308.
- [55] J. A. Pathak, D. Ross, K. B. Migler, *Phys. Fluid.* **2004**, *16*, 4028-4034.
- [56] T. J. Johnson, D. Ross, L. E. Locascio, *Anal. Chem.* **2002**, *74*, 45-51.
- [57] A. K. Singh, E. B. Cummings, D. J. Throckmorton, *Anal. Chem.* **2001**, *73*, 1057-1061.
- [58] S. Devasenathipathy, J. G. Santiago, K. Takehara, *Anal. Chem.* **2001**, *74*, 3704-3713.
- [59] E. McDonnell, S. Han, C. Hilty, K. Pierce, A. Pines, **2005**, in preparation.
- [60] C. Hilty, E. McDonnell, J. Granwehr, K. Pierce, S. Han, A. Pines, **2005**, in preparation.